# research papers

# DESIRS: a state-of-the-art VUV beamline featuring high resolution and variable polarization for spectroscopy and dichroism at SOLEIL

**Laurent Nahon,\* Nelson de Oliveira, Gustavo A. Garcia, Jean-François Gil, Bertrand Pilette,‡ Olivier Marcouillé, Bruno Lagarde and François Polack**

Synchrotron SOLEIL, L'Orme des Merisiers, St Aubin, BP 48, 91192 Gif sur Yvette Cedex, France.
E-mail: laurent.nahon@synchrotron-soleil.fr

DESIRS is a new undulator-based VUV beamline on the 2.75 GeV storage ring SOLEIL (France) optimized for gas-phase studies of molecular and electronic structures, reactivity and polarization-dependent photodynamics on model or actual systems encountered in the universe, atmosphere and biosphere. It is equipped with two dedicated endstations: a VUV Fourier-transform spectrometer (FTS) for ultra-high-resolution absorption spectroscopy (resolving power up to $10^6$) and an electron/ion imaging coincidence spectrometer. The photon characteristics necessary to fulfill its scientific mission are: high flux in the 5–40 eV range, high spectral purity, high resolution, and variable and well calibrated polarizations. The photon source is a 10 m-long pure electromagnetic variable-polarization undulator producing light from the very near UV up to 40 eV on the fundamental emission with tailored elliptical polarization allowing fully calibrated quasi-perfect horizontal, vertical and circular polarizations, as measured with an *in situ* VUV polarimeter with absolute polarization rates close to unity, to be obtained at the sample location. The optical design includes a beam waist allowing the implementation of a gas filter to suppress the undulator high harmonics. This harmonic-free radiation can be steered toward the FTS for absorption experiments, or go through a highly efficient pre-focusing optical system, based on a toroidal mirror and a reflective corrector plate similar to a Schmidt plate. The synchrotron radiation then enters a 6.65 m Eagle off-plane normal-incidence monochromator equipped with four gratings with different groove densities, from 200 to 4300 lines $mm^{-1}$, allowing the flux-to-resolution trade-off to be smoothly adjusted. The measured ultimate instrumental resolving powers are 124000 (174 µeV) around 21 eV and 250000 (54 µeV) around 13 eV, while the typical measured flux is in the $10^{10}$–$10^{11}$ photons $s^{-1}$ range in a 1/50000 bandwidth, and $10^{12}$–$10^{13}$ photons $s^{-1}$ in a 1/1000 bandwidth, which is very satisfactory although slightly below optical simulations. All of these features make DESIRS a state-of-the-art VUV beamline for spectroscopy and dichroism open to a broad scientific community.

## 1. Introduction

VUV photons interacting with gas-phase matter are found in nature, for instance in the interstellar medium or in planetary ionospheres. From a more fundamental point of view, such photon-induced processes are a fine probe of the photon/molecule excitation and relaxation dynamics, and of the structure and stability of matter with a strong relevance in

chemistry, radiobiology and exobiology. It is therefore important to simulate valence-shell photodynamics in the laboratory, *i.e.* the interaction between VUV tunable light and dilute matter. This is why several VUV beamlines have been constructed, following the availability of synchrotron radiation from storage rings. Although some modern bending-magnet VUV beamlines have been operated with fairly high flux (Ito *et al.*, 1995; Song, Ma *et al.*, 2001; Johnson *et al.*, 2009; Giuliani *et al.*, 2009) or high resolution (Ito *et al.*, 1986), VUV beamlines on second- and third-generation sources with

‡ Present address: LCP-MR, 11 rue Pierre et Marie Curie, 75231 Paris CEDEX 05, France.

undulators provide an optimal flux-to-resolution compromise (Koike *et al.*, 1994; Nahon *et al.*, 1998; Song, Tseng *et al.*, 2001; Reichardt *et al.*, 2001; Petaccia *et al.*, 2009; Balasubramanian *et al.*, 2010) and, in some cases, variable polarization (Nahon & Alcaraz, 2004; Tanaka *et al.*, 2009; Derossi *et al.*, 1995; Matsui *et al.*, 2001).

In this paper we present the concept and performance of DESIRS, a VUV undulator-based beamline at SOLEIL, covering the 5–40 eV range for the study of dilute matter (cold molecules, radicals, biological and biomimetic species, clusters and nanoparticles) as well as of condensed matter (thin films and solids). The scientific mission, established to fulfill the needs of a broad and international scientific community, is manifold and includes the following topics:

(i) Very-high-resolution spectroscopy on small molecular systems of astrophysical interest.

(ii) Spectroscopy, fragmentation and reactivity of state- and/or mass-selected molecular cations (and anions) *via* different electron/ion coincidence schemes and the use of ion traps.

(iii) Photoionization dynamics from laser-excited species to clusters and nanoparticles.

(iv) Alignment processes, circular dichroism (CD) and chirality. This large topic takes advantage of the beamline's variable polarization for the study of asymmetric photo-physical and photochemical processes, some of them possibly linked to the origin of life's homochirality.

(v) Excitation and relaxation in solids.

To fulfill this scientific mission, DESIRS was designed for high resolution, spectral purity, *i.e.* no high harmonics contamination, variable polarization including precisely calibrated circularly polarized light (CPL), and high flux, considering that the targets may be very dilute such as trapped ions (Milosavljević *et al.*, 2012). All these properties should be available over the whole VUV range, *i.e.* down to 5 eV and up to 40 eV.

Below we describe the undulator, the constraints taken into account at the optical conception stage, our strategy and the beamline elements, some of them having been transferred and adapted from the former SU5 beamline at Super-ACO (LURE) (Nahon, Alcaraz *et al.*, 2001). Finally the measured performances of the beamline will be presented.

## 2. Source and optical conception

### 2.1. The HU640/OPHELIE2 undulator

The conception, construction and magnetic testing of the HU640 (also called OPHELIE2) undulator has been described elsewhere (Marcouille *et al.*, 2007). Its design has to fulfill two challenging criteria:

(i) Offering a large flux and brilliance down to 5 eV despite the 2.75 GeV nominal electron energy of the SOLEIL storage ring, while keeping a reasonable heat load on the first optics, typically below 120 W in order to have a high temporal stability of the transmitted synchrotron radiation. This translates into low magnetic field peak values, a very long magnetic period and a sufficient number of periods. Considering that

SOLEIL offers four super-long straight sections of 12 m, the optimization of the constraints led to an insertion device with 14 magnetic periods of length $\lambda_0 = 640$ mm with peak magnetic fields of the order of 0.11 T (in the linear horizontal mode), corresponding to a maximum $K$ value of 6.57, with the usual definition

$$K_{x,z} = 0.934\lambda_0 \,[\text{cm}]\, B_{0x,0z}\,[\text{T}], \qquad (1)$$

where $B_{0x}$ (and $B_{0z}$ respectively) is the peak horizontal (or vertical) magnetic field on the axis.

(ii) Allowing the production of controlled ellipses of polarization to adjust for no purely grazing or normal incidence on the optics. Indeed such a geometry induces energy-dependent complex reflectivities (amplitudes and phases) for the *s* and *p* waves incident on the optics, so that in general a non-trivial elliptical polarization must be produced at the undulator level in order to obtain perfect pure CPL at the sample. This requires the production of tunable independent horizontal and vertical magnetic fields with a tunable longitudinal phase shift. In addition, a switching frequency in the AC mode of *ca* 1 Hz was required in the long term for the performance of CD experiments in the VUV with a high signal-to-noise ratio.

These two requirements led us to adopt pure electromagnetic technology and a magnetic scheme with no mechanical motions, based upon three sets of pure air coils (see Fig. 1): a first set generates the horizontal ($B_x$) magnetic field (green coils), while the two other sets (red and blue coils), shifted one from the other by a quarter of a period, generate the vertical ($B_z$) magnetic field with a continuously tunable longitudinal phase shift ($\varphi$) from $-180°$ to $+180°$ with respect to the horizontal magnetic fields. By playing with the three currents driving the coils, one can independently tune $B_{0x}$, $B_{0z}$ and $\varphi$, and therefore produce a tailored elliptical polarization as defined by its three Stokes parameters $S_1$, $S_2$ and $S_3$ (Elleaume, 1994; Nahon *et al.*, 1997). The helicity switching of
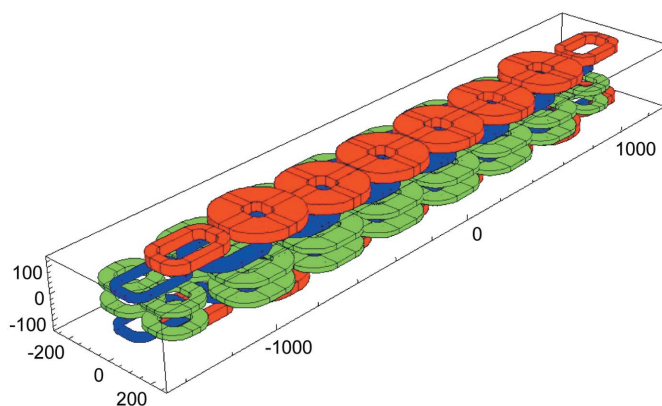


**Figure 1**
Three-period magnetic modeling of the HU640 (OPHELIE2) variable-polarization undulator concept, showing the three sets of pure air coils, generating the vertical and variably phase-shifted horizontal magnetic fields. The actual insertion device has 14 effective periods plus two passive correction periods. Dimensions are in mm.

the CPL is simply achieved by switching the polarity of the current driving the green coils.

## 2.2. Optical design constraints

Based on its scientific mission, DESIRS was designed to provide photons to three independent endstations that should be selected *via* 'OR function' fast switchable mirrors:

(i) A white-beam branch feeding a novel wavefront division-based interferometer Fourier-transform spectrometer (FTS) (de Oliveira *et al.*, 2009). This unique instrument for VUV absorption spectroscopy offers unprecedented resolving power in the $10^6$ range (de Oliveira *et al.*, 2011) over a wide spectral range corresponding to the undulator envelope. This instrument takes advantage of the spatial coherence of the source and requires specific focusing conditions, including vertical focusing in order to enter the tight horizontal slit at the entrance of the FTS. The arm between the deflecting mirror and this slit should also be long enough to accommodate the sample-environment chamber consisting of a windowless gas cell and a molecular beam.

(ii) Two monochromated branches *A* and *B*. On branch *A* the molecular beam endstation SAPHIRS (Richard-Viard *et al.*, 1996) is equipped with an imaging electron/ion coincidence spectrometer (Garcia *et al.*, 2009). Although the electron side is based upon the velocity map imaging concept (Eppink & Parker, 1997), a tight ionization volume is required in order to achieve the best electron resolution as well as mass resolution,

which should be kept below 200 μm in the vertical dimension. Branch *B* is designed to accommodate different experimental chambers from external users. Some of them, because they deal with condensed matter irradiation with controlled photon density (de Marcellus *et al.*, 2011, Meierhenrich *et al.*, 2010) or need precise matching with ion beams (Milosavljević *et al.*, 2011), require a tailored footprint of the synchrotron radiation from a very tight focusing (typically in the 200 μm range) up to ~1 cm² footprint. This variable footprint should be achieved by moving the endstations longitudinally, inducing an extra geometrical constraint on the beamline design and floor plan layout.

In addition, the insertion of a gas filter with conduction-limiting capillaries in order to suppress the undulator high harmonics that would be transmitted by the gratings high orders imposes, as on SU5 (Nahon *et al.*, 1998), the presence of a beam-waist located well before the monochromator. The divergent beam will then have to be refocused onto the entrance slit of the monochromator.

Of course all of these conditions have to be compatible with the general floor plan layout constraints: distance from the source point to the concrete shielding, total available length and the presence of neighboring beamlines.

## 2.3. Optical design

The general optical layout is presented in Fig. 2 and the main characteristics of the optics are summarized in Table 1.
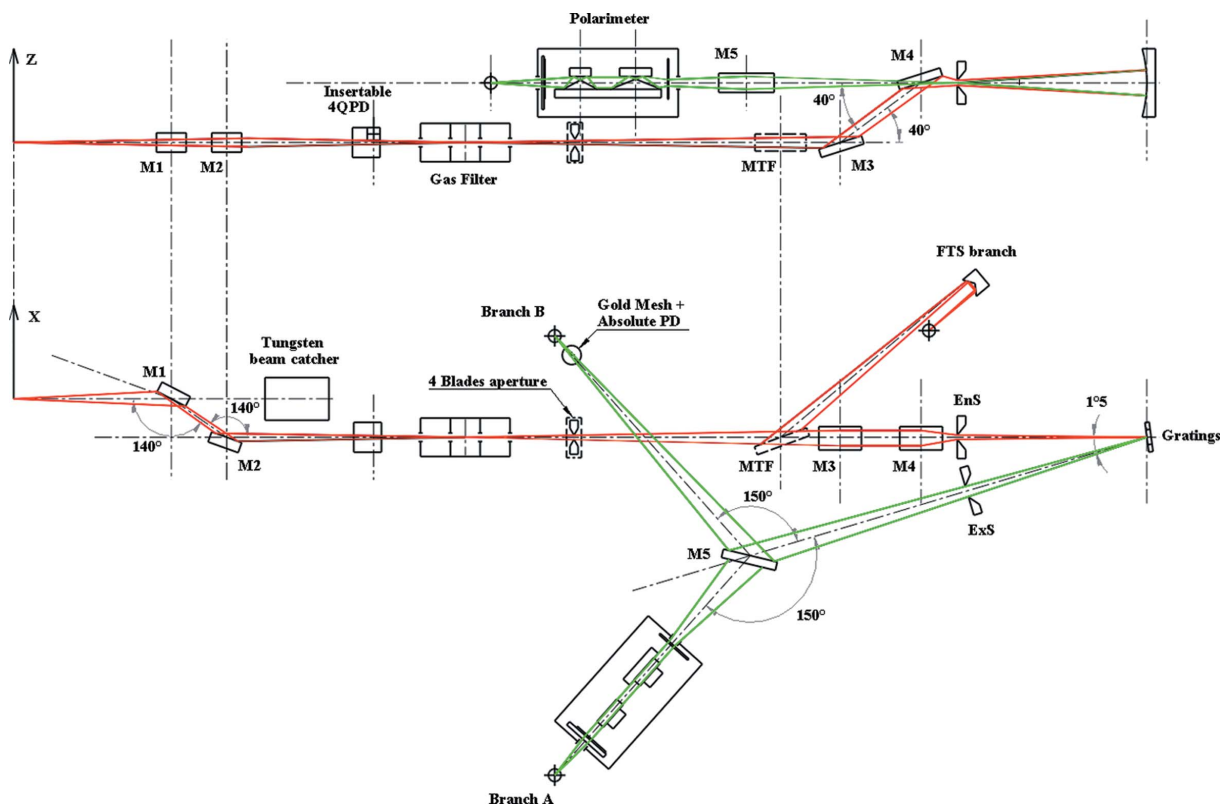


**Figure 2**
Optical layout of the beamline: (top) side view; (bottom) bird's eye view. Red rays (or green rays) correspond to the undispersed white beam (or monochromated beam). 4QPD represents 4-quadrants photodiode, EnS (or ExS) for entrance (or exit) slit.

**Table 1**
Characteristics of the specified beamline optics.

| | Type | Linear dispersion (mÅ) for 100 µm exit slit | Radius (m) | Incidence (°) | Reflective coating/substrate | Distance from the source (m) |
|---|---|---|---|---|---|---|
| M1 | Flat | – | $\infty$ | 70 | –/Si | 20.300 |
| M2 | Toroidal | – | $R = 33.9$ $r = 3.97$ | 70 | –/Si | 20.440 |
| MFT | Toroidal | – | $R = 25.15$ $r = 1.39$ | 70 | –/Si | 42.670 |
| M3 | Pseudo-flat | – | Third-order coeff. 0.058 m$^{-2}$ | 70 | –/Si | 43.641 |
| M4 | Toroidal | – | $R = 4.68$ $r = 3.31$ | 70 | –/Si | 43.874 |
| G1 | Spherical, 200 grooves mm$^{-1}$ | 720 | 6.650 | 0.75 | –/SiC | 51.374 |
| G2 | Spherical, 2400 grooves mm$^{-1}$ | 60 | 6.650 | 0.75 | –/SiC | 51.374 |
| G3 | Spherical, 400 grooves mm$^{-1}$ | 360 | 6.650 | 0.75 | Pt/silica | 51.374 |
| G4 | Spherical, 4300 grooves mm$^{-1}$ | 33 | 6.650 | 0.75 | Pt/silica | 51.374 |
| M5 | Toroidal | – | $R = 22.08$ $r = 0.89$ | 75 | –/Si | 61.024 |

The synchrotron radiation emitted by the undulator impinges onto a first pair of mirrors, M1 and M2, deflecting the beam in the horizontal plane. M1 is planar and takes most of the heat load (up to 120 W), while M2 is toroidal in order to achieve a tight focus ($\sim$0.3 mm diameter) at the gas filter center located $\sim$8 m downstream. The incidence angle (70°) and reflecting material (Si) of M1 and M2 have been chosen so that virtually no photons with energies above 60 eV are transmitted downstream. Therefore, all the heat load is localized onto the first pair of mirrors and is not an issue downstream. Note that the optical chicane achieved by this pair of mirrors allows the positioning on the undulator emission axis of a tungsten block designed to absorb the ionizing radiation from the bremsstrahlung.

After the beam-waist created in the middle of the gas filter, the synchrotron radiation can be steered and refocused towards the FTS endstation by inserting the toroidal MFT mirror for the performance of ultra-high-resolution absorption spectroscopy. For all other types of experiments, this mirror is removed from the beam to let it continue towards the pre-focusing elements (M3 and M4) of the 6.65 m normal-incidence monochromator (NIM). M3 and M4 deflect the beam in the vertical plane with the same incidence (70°) and reflecting material (Si) as M1M2. This deflection therefore balances any effects on the initial polarization state of the light emitted by the undulator, so that the only symmetry breaking between the linear vertical (LV) and horizontal (LH) polarization should be due to the post-focusing M5. This configuration has been chosen so that the photon flux in the LV and LH modes are closely matched. This geometry is also adapted to have the best focusing efficiency on the horizontal entrance slit (EnS) of the NIM.

The high-resolution 6.65 m NIM requires its entrance slit be illuminated with a 1° vertical aperture angle, which is quite large for a 20° grazing-incidence mirror. A simple shape as a toroid is easy to manufacture but produces unacceptable coma aberration. An elliptical stigmatic shape would be challenging to manufacture with the required 850 mm focal length. We have chosen to keep the toroid M4 and apply the shape correction to the otherwise flat mirror M3. This corrector plate includes a meridional S shape (coma correction by a third-degree polynomial) with a height modulation of $\sim$8 µm. The combination of these two mirrors realises a strong demagnification (factor $\sim$18) of the beam in the vertical plane to maximize the flux throughput *via* the entrance slit and to ensure the correct illumination of a maximum number of grating lines. Also, following a concept of astigmatic focusing already implemented on the SU5 beamline (Nahon *et al.*, 1998), M4 gently focuses the beam in the horizontal plane so as to form a thin vertical line footprint on the gratings located 7.5 m downstream of M4. This ensures that a negligible horizontal defocus is induced by the grating's translation during scans, leading to a tight and wavelength-independent beam spot at the experimental points. As can be seen on the ray-tracing simulations shown in Fig. 3, performed with an optimized M3 profile with a 0.058 m$^{-2}$ third-order coefficient, the assumed astigmatism of the M3 + M4 pre-focusing optics leads to a 'smile-shaped' footprint highly focused in the vertical plane at the EnS level, leading to a 63% throughput in a 10 µm EnS at 5 eV. At 15 eV the theoretical throughput rises to 82%.

After M4 the synchrotron radiation enters the Eagle off-plane 6.65 m NIM which has been transferred from the former
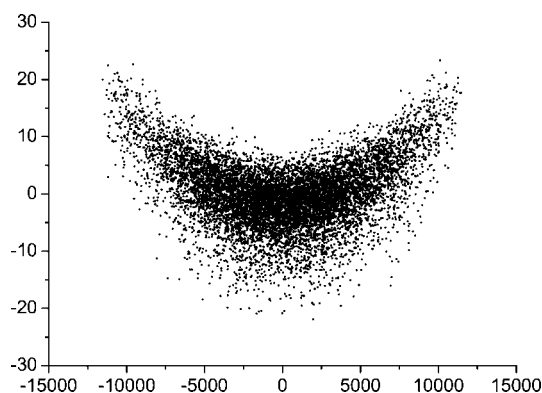


**Figure 3**
Ray-tracing simulation performed at 5 eV, *i.e.* for a maximum divergence of 0.4 mrad at the undulator level, at the entrance slit level, showing a throughput of 63% in a 10 µm entrance slit. Dimensions are in µm.

SU5 beamline at Super-ACO and which has been described in detail elsewhere (Nahon *et al.*, 1998; Nahon, Alcaraz *et al.*, 2001; Nahon, Polack *et al.*, 2001). Briefly, this off-plane mounting, with perpendicular reflection and dispersion planes, ensures a minimum coma aberration while keeping fixed the position of both slits (Namioka, 1959). Wavelength scanning is achieved by rotating and translating the gratings in order to stay on the Rowland cylinder. In addition to the two highly dispersive gratings with 2400 and 4300 grooves mm$^{-1}$, two extra low-dispersion gratings with 200 and 400 grooves mm$^{-1}$ have been added for the performance of flux-hungry experiments on DESIRS. The resolution-to-flux trade-off can be easily adjusted by playing with the slit width and the grating groove density, with the available resolving power (RP = $\lambda/\Delta\lambda$) varying between the 100000 range down to ∼100. Note that it is of course possible to simultaneously scan the gratings and the undulator currents, the so-called 'gapscan', so as to stay at the peak of the undulator emission even in the case of large spectral ranges.

After the exit slit (ExS), the monochromated synchrotron radiation is refocused and steered towards the experimental points *A* or *B* by the toroidal mirror M5. An *in vacuo*, insertable VUV polarimeter transferred and adapted from the SU5 beamline (Nahon & Alcaraz, 2004) has been installed in the branch *A* post-focusing arm, after the last optic and right before the sample environment. This polarimeter concept is based upon the measurement of the transmitted flux after $2 \times 3$ reflections on rotating optical elements (prisms plus flat mirror) acting as a dephaser and an analyzer. Analysis of the flux modulations achieved by independently rotating the two blocks of optical elements along the main synchrotron radiation axis provides, without any assumption, the whole set of Stokes parameters (see §3.6) defining the ellipse of polarization incoming onto the polarimeter. The linear components can be disentangled from the circular one and, in addition, the unpolarized component of light can be determined. In particular, this polarimeter is crucial to build up the undulator setting table, *i.e.* to determine, for a large set of photon energies, the correct polarization ellipse that has to be produced at the undulator level for achieving, after optical modifications, a pure CPL.

### 2.4. Actual beamline components

Here we describe in more detail some of the important actual elements of the beamline. Note that all the optic chambers are mounted on synthetic granite bases, glued to the SOLEIL floor. This mounting appears to be very efficient for suppressing most of the low-frequency vibrations (below 50 Hz).

Just downstream from the front end, inside the optical hutch, at about 20 m from the source, a 13 mm × 13 mm water-cooled square copper diaphragm/absorber selects the radiation in a 0.65 mrad × 0.65 mrad angle, absorbing the extra heat load. In between this diaphragm and the first mirror M1 is located the generic SOLEIL undulator pointing diagnostic DIAGON (Desjardins *et al.*, 2007). In our case this

device is based upon an *in vacuo* insertable Mo/Si multilayer plate and a phosphorescent screen combined, outside a vacuum, with a CCD camera. When the plate is inserted with a 45° incidence, it reflects the synchrotron radiation in a narrow bandwidth around 60 eV. By scanning the undulator magnetic fields it is possible to directly image the different harmonics of the insertion device going through the diaphragm/absorber. With such a device we were able to precisely align and slightly modify the initial survey alignment of the diaphragm/absorber on the undulator magnetic axis with 0.1 mm accuracy. Moreover, and this is a crucial issue, we have been able to check that no remaining uncorrected field integrals, or spurious magnetic defects of the undulator, were important enough to distort the emission pointing by more than ±20 µrad, whatever the undulator setting and polarization mode. Therefore, the required tolerance, especially for the helicity switching in the CPL mode for CD experiments, is achieved by the insertion device.

Great care has been given to the design of the M1M2 chamber (Fig. 4). Indeed, the incoming heat load on M1 can be as high as 120 W so that M1, and to a lesser extent M2, have to be thermalized in order to minimize optics surface deformations. We chose to cryogenically cool M1 with a liquid-nitrogen (LN2) cryosystem. Initially the cryosystem was designed to operate at 96 K, a temperature for which Si, the substrate of M1, shows a vanishing differential thermomechanical deformation coefficient. This was achieved by using a high-pressure liquid/gas nitrogen separator so that liquid nitrogen was maintained at 96 K as a cryocoolant. After two years of operation, because of difficulties in operating this system and since a permanent general circuit of LN2 became available at SOLEIL, it was decided to use a more classical closed-loop system in which 77 K LN2 circulates into the cooling circuit *via* a 2.5 kW cryopump-based system (Cryotherm Gmbh). The
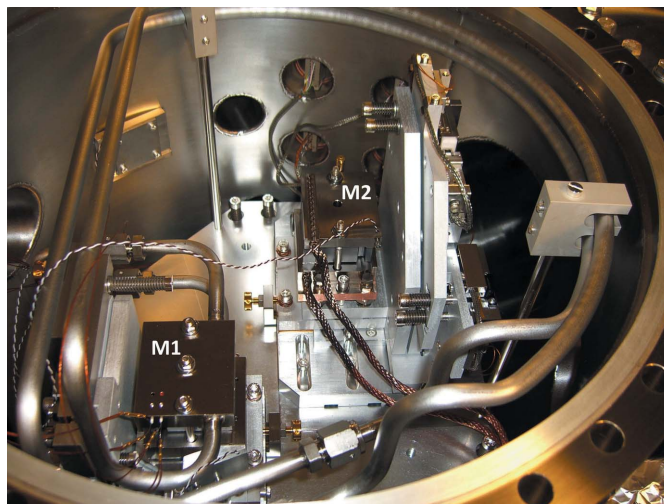


**Figure 4**
Photograph of the M1M2 chamber. The undulator emission comes from the bottom of the picture, hits the M1 flat mirror (left side) and then the toroidal M2 (right side). The cryo-cooling loop connected to the M1 nickel-plated copper heat exchanger can be seen close to the inner wall of the chamber.

LN2 circulation is achieved *via* an *in vacuo* transfer line VCR connected to specially designed copper heat exchangers located on the top and bottom sides of M1. These hollow copper blocks offer a maximum surface for optimizing the heat exchange, and are mechanically clamped to the M1 substrate *via* an indium film. M2 is simply water-cooled at 290 K *via* a copper braid. This solution appears to be very satisfactory. Upon front-end opening, only a small reproducible pointing motion (equivalent to an ∼80 µrad defect of M1) is observed on an insertable beam position monitor (4-quadrant photodiode SXUVPS3, IRD Inc.) located ∼7 m downstream of M2, and becomes stabilized towards the nominal beamline axis within 2 h, whatever the undulator settings.

After M2 the beam is focused onto the center of the gas filter, which has been transferred from SU5 (Mercier *et al.*, 2000) and adapted to DESIRS. Triple differential pumping is achieved by four 1.5 and 1.9 mm internal diameter 10 cm-long conductance-limiting capillaries, so that typical pressures of up to 0.5 mbar of Ne, Ar, Kr or Xe over an effective absorption length of 15 cm can be injected in the central part of the filter, while maintaining UHV conditions in the external parts connected to the beamline pipes. According to Beer–Lambert's law and to our experimental measurements, the achieved absorption column density is high enough to suppress the high harmonics of the undulator by four to five orders of magnitude (Mercier *et al.*, 2000). By filling the gas cell with different rare gases corresponding to different ionization potentials, *i.e.* different energy cut-offs, it is possible to produce harmonic-free radiation from 6 to 21 eV. Note that below the cut-off energy the gas filter is 100% transparent, which is absolutely not the case for MgF$_2$ or LiF windows, often used instead of a gas filter. Indeed, these materials exhibit high absorption due to defects in the material, such as color centers for instance, even below their energy cut-off. Above 21 eV there is no need for any harmonic suppression since the gratings at normal incidence do not transmit many photons above 42 eV. Compared with the filter operation on SU5 at Super-ACO (LURE, Orsay), because of the much lower emittance of SOLEIL, and despite the diffraction limit, the beam FWHM transverse dimensions in the filter are of the order of 150 µm (V) × 300 µm (H) so that the alignment is much easier and the photon density of the white beam is high enough to ignite a spectacular plasma radiating in the visible spectrum, as seen in Fig. 5. We assume ∼100% transmission of the beam through the filter capillaries.

A four-blade aperture chamber which allows the beam aperture angle that will be used downstream to be tuned is installed 5 m downstream from the filter, on the beamline arm where both the horizontal and vertical divergences are of ∼1 mrad. For polarization-dependent experiments, or for white-beam irradiation experiments requiring as narrow a white spectrum bandwidth as possible, the blades are adjusted so that only the central cone of the undulator emission is collected, otherwise they can be set wide open. These blades are also used to tailor the transverse footprint of the beam for
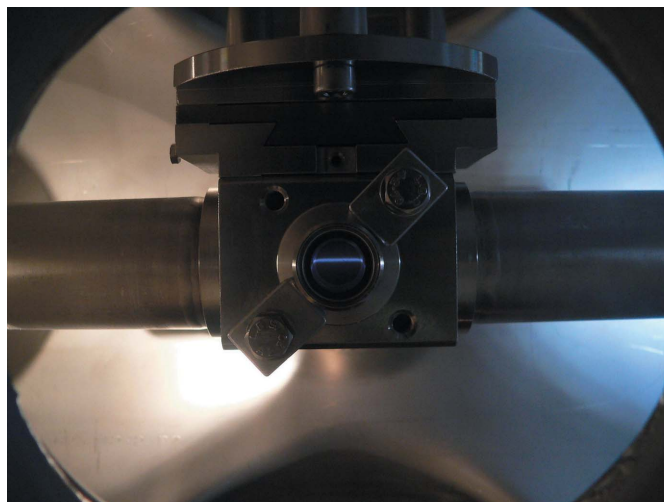


**Figure 5**
The line-shaped rare-gas plasma ignited by the white synchrotron radiation beam from the undulator, observed in the central section of the gas filter filled with Xe through the survey viewport. The typical transverse dimensions of the beam are 150 µm (V) × 300 µm (H).

some experiments requiring large footprints and positioned after the experimental focal point on branch *B*.

Special care has been paid to the manufacturing of the M3 correcting plate, whose third-degree polynomial shape has been realised by SAGEM-REOSC by ion etching from a flat Si substrate. The achieved surface shape, as measured at SOLEIL by a long-trace profilometer, has a third-degree coefficient of 0.0622 m$^{-2}$, which is slightly different from the 0.058 m$^{-2}$ specification. Owing to this slight over-correction, the ray-tracing simulation of the actual combination yields a slightly lower throughput after the EnS, *e.g.* 73% rather than the expected 82% at 15 eV for a 10 µm slit.

The post-focusing mirror M5 is mounted onto a one-axis goniometer, actuated by ceramic motors (Nanomotion) achieving a highly reproducible rotation around the vertical axis. This motion is used over a very large angle (150°) when the beam is switched from experimental point *A* to *B*. This happens quite often in order to mount and pre-align an experimental chamber on branch *B*, for an hour or so, while an experiment is running on branch *A*. In practice the branch switching is done in less than a minute with a reproducibility better than 3 µrad in the horizontal plane and 1.5 µrad in the vertical plane, which is very satisfactory. The same rotation motion is also used to compensate, at the experimental point, for the slight horizontal motion induced by the grating's translation during a scan due to the off-axis geometry of the monochromator.

Finally, the beamline is equipped with a whole series of diagnostics to measure the initial performances of the beamline and to monitor them in time: gold meshes and ZnS fluorescent screens at several locations in the white and dispersed arms, as well as calibrated photodiodes (AXUV, IRD Inc.) in the differential pumping chamber located in the post-focusing arms on both *A* and *B* branches.

**Table 2**
Energy range of the HU640 electromagnetic undulator fundamental radiation for the different polarization modes.

| Polarization mode | Active sets of coils† | Covered energy range (eV) |
|---|---|---|
| LH | Blue and red | 2.8–40 |
| LV | Green | 6.3–40 |
| Calibrated CPL | Green, blue and red | 4.5–40 |
| Uncalibrated elliptical | Green, blue and red | 2.0–40 |

† See Fig. 1.

## 3. Performance

### 3.1. Energy range of the beamline

In the vertical linear polarization mode, a $K_X$ value of $\sim 5.8$ corresponding to a minimum energy of 6.3 eV can be reached by driving the 'green' coils at the highest possible current (600 A; see Fig. 1) of the OPHELIE2 undulator. In the linear horizontal mode, by driving the 'blue' and 'red' coils to their maximum current (440 and 360 A), a $K_Z$ value of about 8.89 can be reached, corresponding to a minimum energy of 2.77 eV, *i.e.* in the visible region. Note that these low-energy limits, summarized in Table 2, are in excellent agreement with simulated spectra taking into account the $K$ values derived from actual magnetic measurement. The linear vertical polarization has a slightly higher transmission by the beamline optics (between 40% and 5% depending on the photon energy) and is used on the FTS branch for which a 6.3 eV minimum working energy is very satisfactory, and complementary to the available UV FTS techniques. The linear horizontal polarization is most important for the monochromator branch allowing access to electron- or ion-angular distributions with the position-sensitive detector of DELI-CIOUS2 lying in the horizontal plane (Garcia *et al.*, 2009). In all cases, the design specifications are largely met and the ability to go below 5 eV is greatly appreciated to study photon-induced processes over a very broad spectral range (UV and VUV), photoluminescence in material sciences, photodetachment on anions (Milosavljević *et al.*, 2012) or even photoemission from large systems such as nanoparticles (Gaie-Levrel *et al.*, 2011). The minimum energy available in the calibrated CPL mode is 4.5 eV, although, if needed and by setting all power supplies to their maximum current, one can reach a total $K$ value leading to an uncalibrated elliptical polarization with an energy of 1.96 eV, *i.e.* in the red. In practice this ability to reach the visible range was extremely useful during the initial in-air alignment of the beamline. Note that the monochromator can disperse radiation down to 4 eV with the 2400 grooves mm$^{-1}$ high-resolution grating and down to the IR region with the low-dispersive 200 grooves mm$^{-1}$ grating.

Finally we find that the flux crossing point between the fundamental and the third harmonic of the undulator emission is in the 35–40 eV region; therefore, in practice we operate the undulator on the fundamental over the whole VUV range covered by the beamline, *i.e.* up to 40 eV. Its computer control is hence much simpler, for instance, than it was with the SU5

undulator (Nahon & Alcaraz, 2004) which was used on several successive harmonics.

### 3.2. Throughput *via* the entrance slit

In order to maximize the photon flux in the case of high-resolution experiments, one of the crucial issues is to ensure optimal photon throughput *via* the EnS, taking advantage of the very small vertical emittance of SOLEIL. This is the role of the pre-focusing system M3M4. After careful *in vacuo* vertical alignment of M4, we measured the photon throughput at 15 eV *via* EnS, using a gold mesh, as shown in Fig. 6. Although the delivered M3 corrector mirror does not have the exact specified shape (third-degree coefficient 0.0622 m$^{-2}$ rather than 0.058 m$^{-2}$), the results are very satisfactory: 90% throughput for a 20 µm slit and 60% for 10 µm. This is close to the optical simulations made with the actually measured M3 shape which give 95 and 73% for 20 and 10 µm slits, respectively. In addition, the satisfactory fitting with an error function, as depicted in Fig. 6, shows that the synchrotron radiation footprint is not far from a Gaussian profile in the vertical plane with an FWHM of 14 µm. This value is totally compatible with the fully diffraction-limited vertical size of the source of 230 µm (FWHM) at 15 eV which, after demagnification by a factor of $\sim 18$, gives a $\sim 13$ µm FWHM size at the EnS position. Basically, all photons are collected within a 40 µm EnS. Compared with the SU5 beamline (Nahon, Alcaraz *et al.*, 2001) installed on the second-generation storage ring Super-ACO, on which the spot size at the EnS location was mainly electron emittance-limited, for the 10 and 20 µm slits the throughput has been multiplied by a factor of five, and even for a 60 µm slit by a factor of two.

### 3.3. Focal point size

The size and shape of the focal points on the monochromated branches have been observed with a simple optical system monitoring the zeroth-order radiation, in the near UV
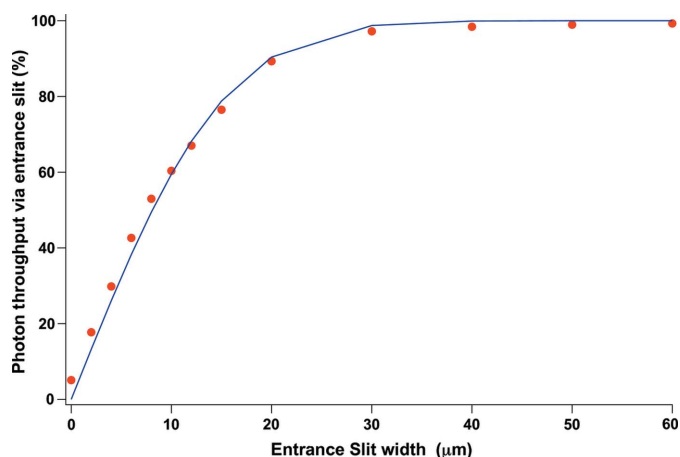


**Figure 6**
Measured photon throughput of the undulator emission centered at 15 eV *via* the entrance slit as a function of the slit width (circles), normalized to 100% at 150 µm. The solid line corresponds to a fitting with an error function, showing that the synchrotron radiation footprint at the EnS position has a quasi-Gaussian shape with a 14 µm FWHM.
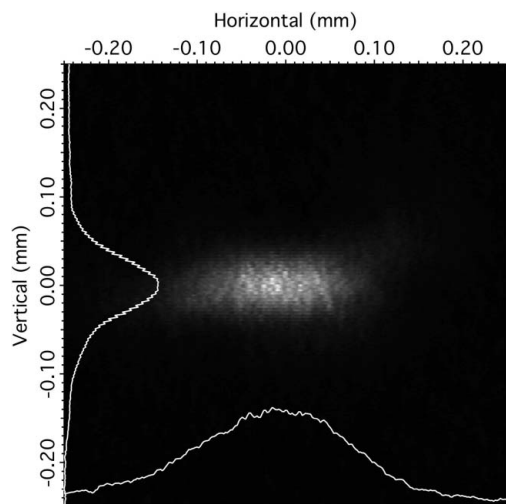
**Figure 7**
CCD camera image and profile of the zeroth-order radiation measured at the focal point of the monochromated branches for a 3.2 eV photon energy setting of the undulator. A two-dimensional Gaussian fitting provides a FWHM size of 78 µm (V) × 203 µm (H). Optical densities and multilayer filters were used to avoid saturation and mixing with the spurious bending-magnet radiation.

region (3.2 eV), as it impinges in air onto a ZnS screen with the fluorescence imaged onto a CCD camera. Optical densities and multilayer-based filters have been used to avoid any saturation effects and to isolate the undulator emission from the residual bending-magnet radiation. Note that such an imaging experiment was also used to calibrate the M5 rotation in order to correct for the small position slippage at the exit slit level, due to the off-plane design of the NIM, as a function of the grating's translation, *i.e.* of the selected wavelength. The beam profile at the focal spot, as shown in Fig. 7, is quasi-elliptical with a horizontal major axis. This pattern can be fitted quite nicely with a two-dimensional Gaussian function, leading to a measured FWHM size of 78 µm (V) × 203 µm (H) which is very satisfactory for our purpose and which should be even smaller at higher energy. This measurement was carried out for 30 µm EnS, *i.e.* by taking ∼100% of the incoming photons through the EnS, which were imaged by the grating onto the ExS, here wide open. So this size can be considered as the minimal size of the beam at the focal spots *A* and *B*. When the monochromator is working in first order, the vertical size has to be convoluted with the actual exit slit, which will be dominant above ∼100 µm slit aperture.

The divergence of the beam at the focal spot locations *A* and *B*, typically 5 mrad (H) × 13 mrad (V), is very convenient to increase, when needed, the synchrotron radiation footprint size up to the cm$^2$ range by moving the sample downstream by a meter or so, which is compatible with the beamline floor plan layout.

### 3.4. Spectral resolution

This section describes the high spectral resolution that can be achieved by the 6.65 m NIM equipped with its two highly dispersive gratings: G2, the 2400 lines mm$^{-1}$ grating (uncoated SiC) optimized for the 4–20 eV range, and G4, the 4300 lines mm$^{-1}$ grating (Pt-coated silica) optimized for the 15–40 eV range. The general capabilities (wavelength scanning, resolution *versus* slits, absolute calibration) of this NIM equipped with the same two gratings, installed on the former SU5 beamline, have been described in great detail elsewhere (Nahon, Alcaraz *et al.*, 2001). We focus here only on the ultimate resolution potential capabilities brought by its implementation on the DESIRS beamline at SOLEIL. Note that the Doppler broadening contribution to the linewidths has been neglected since the experiments have been performed on the molecular jet set-up of the SAPHIRS experiment, giving a peaked distribution of the gas velocities perpendicular to the synchrotron radiation propagation axis.

The 4300 lines mm$^{-1}$ grating (G4) was tested on Ne. In Fig. 8 we show an autoionization spectrum (total ion yield) recorded in between the two $2p^{-1}$ thresholds with a 5 µm entrance slit/ 10 µm exit slit and with the absolute scale calibrated according to Ito *et al.* (1988). This spectrum shows excellent long-term stability over the ∼3 h-long acquisition. Since the $18s'$ autoionizing line has a very narrow natural width of 9 µeV (Klar *et al.*, 1992), it is possible to directly fit a Gaussian profile, as shown in the insert of Fig. 8, leading to an instrumental
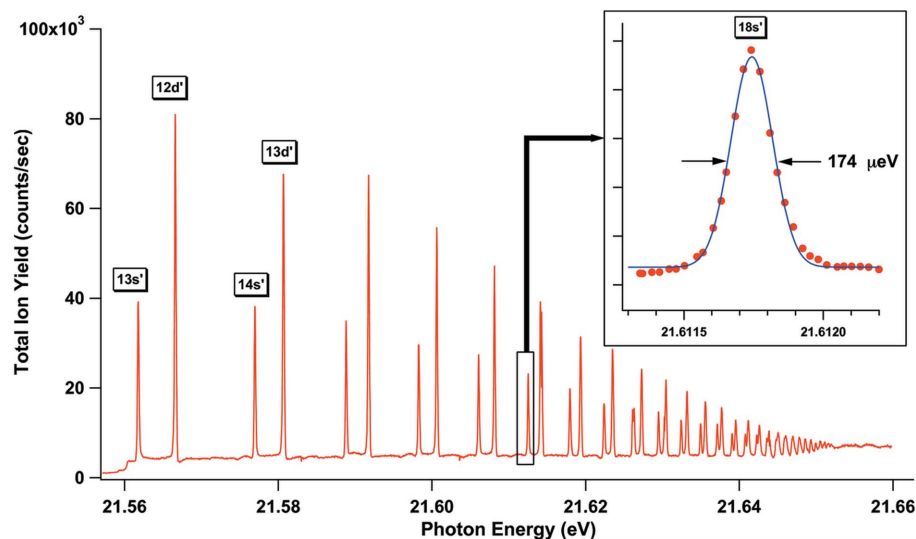


**Figure 8**
Autoionization spectrum of Ne (total ion yield) recorded between the two $2p^{-1}$ thresholds with a 5 µm entrance slit/10 µm exit slit (30 µeV steps, 2 s per point) and 4300 lines mm$^{-1}$ grating. The insert shows a blow-up of the $18s$ resonance and an instrumental Gaussian fit showing a 174 µeV linewidth (resolving power 124000). Note that the $13s$ resonance appears here in the ionization continuum because of the DC Starck shift induced by the rather high electric field applied to repel ions, lowering the ionization threshold.

bandwidth of 174 µeV, corresponding to a resolving power of 124000 (note that closing the ExS down to 5 µeV does not change this ultimate resolution). This is a slightly better performance than obtained on SU5 with 8 µm slits (184 µeV), showing that, as already pointed out, the ultimate resolution with this grating (4.6 mÅ here) is mainly limited by the slope errors (0.8 µrad) below 15 µm slits. Nevertheless, to our knowledge, this resolving power is the highest ever published in this energy range for a scanning monochromator, although very close to the achieved resolution (187 µeV) obtained on the 10 m NIM at BESSYII (Reichardt et al., 2001; Balzer et al., 2004). At lower photon energies, the limitations induced by the slope errors of the 4300 lines mm$^{-1}$ grating are less severe (for a given resolving power) so that on the 16$s'$ line of Xe around 13.34 eV it has been possible to reach an instrumental state-of-the-art resolving power of 249000 (53 µeV) by closing the slits down to 5 µm, a significant improvement when compared with the value of 188000 (71 µeV) obtained on SU5 (Nahon, Alcaraz et al., 2001). Note that such small slits on SU5 were simply not possible to use in practice because of the very low photon throughput via the EnS.

The 2400 lines mm$^{-1}$ grating (G2) was tested on several rare gases including Xe, whose autoionization spectrum of the 16$s'$ line was obtained with slits of 5 µm (Fig. 9) after absolute energy scaling according to Yoshino & Freeman (1985). By fitting a Voigt profile to the raw data (95 µeV FWHM) it is possible to deconvolute an instrumental Gaussian linewidth of 56 µeV from the finite lifetime of this Rydberg state (61 µeV; Klar et al., 1992), corresponding to a resolving power of 238000 instead of an ultimate resolving power of 155000 on SU5 with 10 µm slits. The corresponding spectral width (3.9 mÅ) has been dramatically reduced compared with SU5 (6 mÅ) by closing the slits from 10 to 5 µm, showing that in the case of G2, featuring much smaller slope errors (0.47 µrad),
the ideal pure slit-limited bandwidth behavior is maintained well below 10 µm slits. This slit closing was possible on DESIRS because of the low emittance of the source and the performances of the pre-focusing optical system (see §3.2).

Finally, note that the 200 lines mm$^{-1}$ (G1: uncoated SiC optimized for the 5–20 eV range) and 400 lines mm$^{-1}$ (G3: Pt-coated silica optimized for the 18–40 eV range) low-dispersion gratings show a moderate slit-limited resolution down to 30 µm slits for G1 and down to 15 µm slits for G3. For smaller slits, their non-optimized slope errors (1.9 and 1.0 µrad) dominate. G1 and G3 can therefore cover typical resolving powers (RP) in the 10000 to 100 range, depending on the photon energy and of the slit
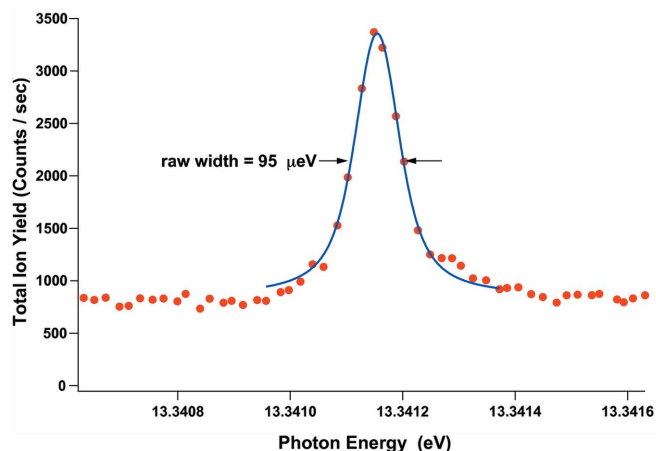


**Figure 9**
Autoionization spectrum of the 16$s$ line of Xe recorded with 2400 lines mm$^{-1}$ grating and 5 µm slits (20 µeV steps, 1 s per point). The solid line shows a Voigt profile fitting yielding a Gaussian FWHM instrumental resolution of 56 µeV linewidth (resolving power 238000). The background is due to the underlying 14$d$ broad resonance.

width, achieving resolution which is very complementary to that obtained with the two highly dispersive gratings.

### 3.5. Absolute flux

A summary of the flux performances of DESIRS is presented in Fig. 10, showing for the four gratings the absolute available flux measured at the sample location with a calibrated Si photodiode (AXUV100, IRD, calibrated at the PTB in Berlin). The data correspond to a 'high resolution' 1/50000 bandwidth for the highly dispersive gratings G2 and G4, and to a 'low resolution' 1/1000 bandwidth for the low dispersion gratings G1 and G3. In practice the data have been recorded with fixed 100 µm slits and scaled to provide the desired
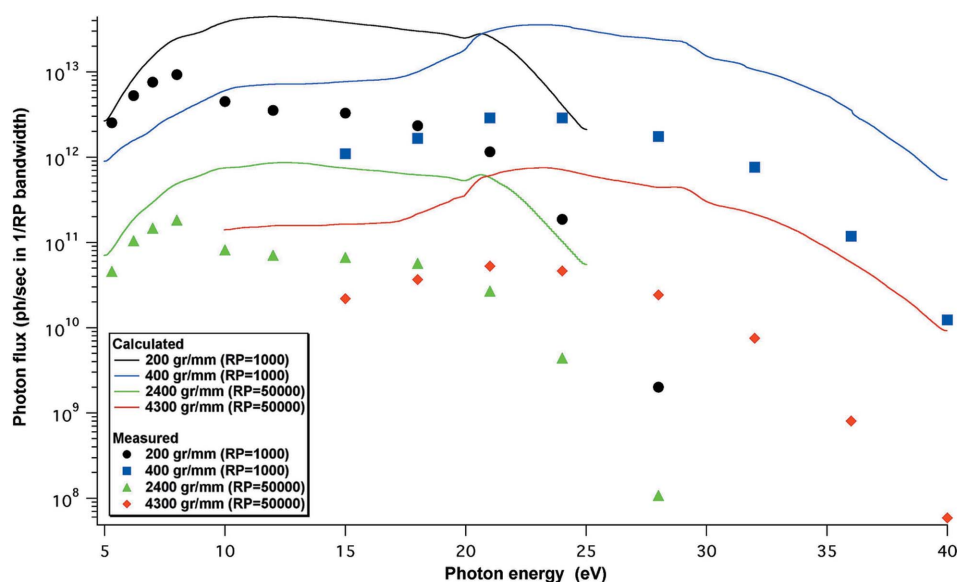


**Figure 10**
Absolute harmonic-free photon flux for a 500 mA current within the full beamline aperture (0.65 mrad × 0.65 mrad) in the linear vertical polarization mode for the four gratings of DESIRS with different resolving powers (RP). Symbols correspond to the measured data (Si photodiode) and lines correspond to optical simulations.

bandwidth. Note that the flux for different interpolated or extrapolated bandwidths can be obtained by a simple linear scaling, considering that this figure is only exit-slit-limited because of the very small synchrotron radiation footprint at the EnS level.

Over the 5–32 eV range the typical flux is $10^{10}$–$10^{11}$ photons s$^{-1}$ in a 1/50000 bandwidth and $10^{12}$–$10^{13}$ photons s$^{-1}$ in a 1/1000 bandwidth before falling to lower values above 32 eV, a decrease mainly due to the low reflectivity on the normal-incidence gratings at high energy. Also, as expected above 20 eV, the Pt-coated gratings deliver higher flux than the uncoated SiC gratings. Comparison with optical simulations taking into account the calculated first-order diffraction efficiencies from the AFM-measured actual gratings groove profiles, and the reflectivities of all the optics with optical data from the literature (optical constant tables extracted from *XOP* software distribution, see http://ftp.esrf.eu/pub/scisoft/xop2.3/DabaxFiles/) is quite interesting. At low photon energies (below 10 eV), agreement between the measurements and the simulation is quite satisfactory while with increasing energy the measured data are about an order of magnitude below the simulations. This trend cannot be explained by some limiting angular apertures on the beamline, which would favor high photon energies. It is also not linked to the gratings, since for a given photon energy the ratio between the calculated and measured flux appears to be of the same magnitude for the four gratings. This discrepancy may have a double origin:

(i) An overestimation of the Si reflectivity from the literature data, possibly due to the fact that the crystalline state considered in these data may not be fully representative of the actual surface layer of our polished silicon mirror. Even a small discrepancy can have a dramatic effect, considering that five Si mirrors have to be taken into account.

(ii) Losses in the measured flux may be due to carbon contamination of the optics. Indeed since the beginning of the DESIRS operation in 2008 some severe variations in the transmitted flux, especially in the 9–14 eV range, were noticed that were clearly due to C-contamination. The contamination affected more specifically the H or V linear polarization according to the contamination level on M1M2 or M3M4 (Yao-Leclerc *et al.*, 2011). During the first years of operation of DESIRS the first four mirrors were cleaned by an *in situ* oxygen RF plasma source (GV10x, IBBS) and the G1 and G2 gratings by *ex situ* UV lamp active oxygen generation. This allowed recovery of the maximum flux and now, after more than four years of intensive operation and conditioning of the UHV chambers, the rate of C-contamination seems quite low. However, it is likely that residual contamination is probably still present on some of the optics, which may decrease the measured flux.

Despite the lower than modeled flux, the measured flux level is very satisfactory, allowing the achievement of the whole initial scientific program. A comparison with the flux obtained on SU5 shows the improvement achieved by moving from Super-ACO to SOLEIL. In a 1/50000 bandpass, the gain in flux is of the order of a factor of three at low energy up to a

factor of ten or more at 32 eV and above. This is partly due to the higher number of undulator periods at SOLEIL (14 periods *versus* 10), but mostly this is due to the much higher photon throughput *via* EnS at SOLEIL, an advantage which increases with increasing energy. Compared with high-flux bending-magnet beamlines such as the 3 m NIM at the Photon Factory (Ito *et al.*, 1995) or the 6 m cylindrical grating monochromator (CGM) at Taiwan Light Source (Song, Ma *et al.*, 2001), the DESIRS harmonic-free flux in a low RP of 1000 is either comparable with the harmonic contaminated CGM flux or 5–10 times higher than the 3 m NIM flux, and orders of magnitude higher when high RPs are considered. This simply reflects the much higher brilliance of undulator sources. Compared with the 10 m NIM high-resolution undulator beamline at BESSYII, the DESIRS flux is higher by a factor of 30–2 depending on the energy range, and whether at BESSYII one considers the harmonic-free (achieved by inserting a LiF filter) radiation or not (Baumgärtel, 2011). Finally, compared with the undulator-based beamline involving the former 6 m NIM at the Advanced Light Source (ALS) (Heimann *et al.*, 1997), in a high-resolution RP of 25000 the flux on DESIRS is higher by a factor of 2–5, the lower emittance of SOLEIL compensating for the higher number of periods of the ALS undulator.

### 3.6. Polarimetry

One of the features of DESIRS is the variable polarization capability of the undulator associated with the ability of measuring the polarization ellipse *in vacuo* at any time (within typically 30 min), just upstream of the sample, with a dedicated VUV polarimeter (Nahon & Alcaraz, 2004). To our knowledge, DESIRS is the only variable polarization beamline in the world equipped with such a permanently available device. This allows full disentanglement of the polarization as given by its Stokes parameters decomposition,

$$\left(S_1^2 + S_2^2 + S_3^2\right)^{1/2} + S_4 = 1, \qquad (2)$$

where $S_1$ is the normalized linear component on a vertical/horizontal axis, $S_2$ is the normalized linear component on a 45/135° tilted axis, $S_3$ is the normalized circular component (with the convention $S_3 > 0$ for the right-handed CPL) and $S_4$ is the normalized unpolarized component. Such a measurement is critical in order to build up the calibration table in the CPL mode of operation, to check for the effect of carbon contamination onto the absolute polarization rate by determining the unpolarized Stokes component $S_4$, as well as to know the absolute circular polarization rate $S_3$ needed to normalize CD signals (Nahon *et al.*, 2006). Fig. 11 shows three examples of polarization ellipses recorded at 20 eV. The ellipses 'LV' and 'LH' have been recorded in the pure LV and LH linear polarization modes, *i.e.* by using only the green or the blue/red coils (see Fig. 1). These measurements are extremely satisfactory since they correspond to quasi-perfect linear polarization with an absolute normal linear component $S_1 \simeq \pm 0.99$. This is the case at any photon energy and no specific polarization calibration in this linear mode is needed
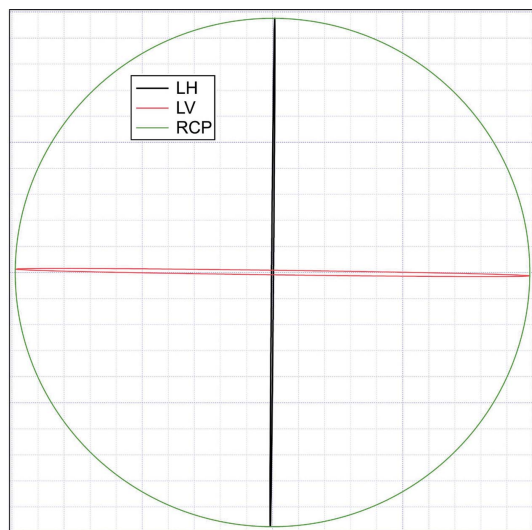
**Figure 11**
Measured polarization ellipses, as recorded with the *in situ* and *in vacuo* VUV polarimeter, at 20 eV for different polarization modes: linear vertical (LV) polarization with $S_1 = -0.99$; linear horizontal (LH) polarization with $S_1 = +0.99$; right-handed CPL (RCP) for which the measured absolute circular polarization rate $S_3$ is 0.99. Over the whole VUV range the measured absolute values of $S_3$ are in the 0.97–0.99 range for both helicities.

since the H and V axis corresponds to the main symmetry axis of all the beamline optics. This was not the case for instance on SU5, where the first mirror produced a dual vertical and slightly off-horizontal plane reflection leading to some tilting of the linear polarization (Nahon & Alcaraz, 2004).

The situation is more complicated for the CPL mode of operation since one has to determine which polarization ellipse of undulator emission leads to a purely left- or right-handed CPL (l-CPL and r-CPL) at the sample location. The procedure, to be repeated for a large number of photon energies spanning the whole VUV range, is the following: from a guessed ellipse of undulator polarization one measures the transmitted ellipse at the sample location with the polarimeter. Departure from a perfect CPL, in terms of H/V amplitude ratio ($\neq 1$) and phase shift ($\neq \pm 90°$), is analyzed and compensated for *via* the undulator computer control system in which the relationships between the magnetic fields and the Stokes parameters of the emitted light have been implemented. Within a single iteration it is possible to minimize the residue of linear component ($S_1$ and $S_2$) to a negligible amount (below 1 or 2%), leading to a quasi-perfect CPL, as shown in Fig. 11 ('RCP' ellipse) where $S_3 = 0.99$. This shows that the insertion device behaves as expected from the helical undulator algebra (Elleaume, 1994; Nahon *et al.*, 1997). We also checked that the helicity switching of light is simply achieved by inducing a 180° phase shift of the horizontal magnetic field by switching the polarity of the current driving the green coils, leading to the same absolute value of $S_3$ within the polarimeter error bars (of the order of $\pm 1$%). Note that this switching is currently done within $\sim 20$ s (DC mode), a figure which should be reduced to $\sim 1$ s in the near future (AC mode).

The polarimetry procedure was applied at various photon energies to construct the initial CPL calibration table, which was checked and updated with time. These checks were especially important at the beginning of the beamline operation, because the evolving C-contamination of the optics was affecting the horizontally (M1M2) or vertically (M3M4) deflecting mirror pairs differently, leading to strongly varying ellipses (H/V ratio and phase) that we had to compensate for. In addition to changing the polarization ellipse, another C-contamination effect was observed regarding the absolute polarization rate in the CPL mode ($1 - S_4$). Indeed, at a time when the beamline was strongly C-contaminated, we observed at some photon energies (especially in the 8–14 eV range) a high level of unpolarized light with $S_4$ coefficients reaching up to 20%. We attribute this effect to a variable phase shift between the *s* and *p* components of light, induced by the non-homogeneous variable thickness of the C-film deposited mainly on the cryogenically cooled first mirror (Chauvet *et al.*, 2011) which cannot be compensated for by a single phase shift of the undulator. When the same polarimetry measurement was performed by selecting a very narrow solid angle around the main axis (about 20% of the central cone) with the four-blade aperture chamber, the $S_4$ parameter decreased to a few % because of the much more homogeneous sampled C-film thickness coating the beamline optics. Nowadays, with a much lower C-contamination rate and absolute level, even on a quite large solid angle such as the central cone of the undulator emission, the unpolarized contribution $S_4$ is below 3%. In addition, the vertical-to-horizontal amplitude ratio and longitudinal phase shift vary smoothly with the photon energy, as expected from optical simulations.

Presently, the absolute circular polarization rates $S_3$ in the CPL mode, which are the actual figures of merit for the different type of CD experiments performed on the beamline, are known to be above 97% over the whole VUV range, and reaching 99% on most of the VUV range. They are mainly limited by a spurious $S_4$ contribution probably due to the remaining slight C-contamination on the optics. As a result DESIRS is today fully calibrated for the four 'normal' modes of operation (LV, LH, r-CPL and l-CPL) in the 4.5–40 eV range, with an undulator operation totally transparent for the users.

A comparison with other undulator-based variable-polarization VUV beamlines clearly shows that DESIRS is established today as state-of-the-art in this field. Indeed, compared with SU5 (Nahon & Alcaraz, 2004), the degree of polarization obtained on DESIRS is higher in both the linear and the circular polarization cases, and the whole VUV range can be covered, which was not the case on SU5 in the CPL mode. Compared with the CIPO beamline at Ellettra (Derossi *et al.*, 1995), the $S_3$ achieved on DESIRS are much higher. This is due to the limited magnitude of the horizontal magnetic field of the elliptical wiggler used on that beamline which flattens the polarization ellipses in the VUV range, limiting $S_3$ to 75% at 8.4 eV (Desiderio *et al.*, 1999) and 50–90% over the VUV range depending on the photon energy and the ring energy, as measured by an indirect method (Nahon *et al.*, 2006). As for

the BL-5B beamline at the TERAS storage ring (Tanaka *et al.*, 2009) using an Onuki-type four-period undulator (Onuki, 1986) as a source, the available absolute circular polarization rates are limited to 85% at 6 eV down to 45% at 30 eV mainly because of the non-compensation of the beamline optics effects over the emitted CPL from the undulator.

## 4. Conclusion

The DESIRS VUV beamline is based upon a complex but efficient design, taking advantage of the very low emittance of the SOLEIL storage ring. The high energy of the ring (2.75 GeV), which may not be ideal for covering the VUV range, imposed the use of a unique very long variable polarization insertion device, together with an original heat-load handling strategy and an efficient high-harmonic-suppressing system. Great care was taken at all levels, including mechanical vibrations, optical manufacturing and alignment or control command. This leads to a state-of-the-art beamline featuring very high energy resolution, flux, spectral purity, a tight focus and variable well calibrated, quasi-pure polarizations even in the challenging CPL mode of operation. In early 2008 this beamline was open to a wide international user community. Since then, an average of ∼28 projects per year are achieved by users with an average of 160 days of beam time per year available to external users and in-house research.

## References

Balasubramanian, T., Jensen, B. N., Urpelainen, S., Sommarin, B., Johansson, U., Huttula, M., Sankari, R., Nommiste, E., Aksela, S., Aksela, H. & Nyholm, R. (2010). *AIP Conf. Proc.* **1234**, 661–664.

Balzer, A., Follath, R., Reichardt, G., Ehresmann, A., Klumpp, S., Molter, H. & Schmoranzer, H. (2004). *First Commissioning Results of the U125/2-10m-NIM.* 2003 Bessy Annual Report, pp. 517–519. BESSY, Berlin, Germany.

Baumgärtel, P. (2011). Personal communication.

Chauvet, C., Polack, F., Silly, M. G., Lagarde, B., Thomasset, M., Kubsky, S., Duval, J. P., Risterucci, P., Pilette, B., Yao, I., Bergeard, N. & Sirotti, F. (2011). *J. Synchrotron Rad.* **18**, 761–764.

Derossi, A., Lama, F., Piacentini, M., Prosperi, T. & Zema, N. (1995). *Rev. Sci. Instrum.* **66**, 1718–1720.

Desiderio, D. *et al.* (1999). *Synchrotron Radiat. News*, **12**, 34–38.

Desjardins, K., Hustache, S., Polack, F., Moreno, T., Idir, M., Dubuisson, J. M., Daguerre, J. P., Giorgetta, J. L., Thoraud, S., Delmotte, F. & Ravet-Krill, M. F. (2007). *AIP Conf. Proc.* **879**, 1101–1104.

Elleaume, P. (1994). *J. Synchrotron Rad.* **1**, 19–26.

Eppink, A. T. J. B. & Parker, D. H. (1997). *Rev. Sci. Instrum.* **68**, 3477–3484.

Gaie-Levrel, F., Garcia, G. A., Schwell, M. & Nahon, L. (2011). *Phys. Chem. Chem. Phys.* **13**, 7024–7036.

Garcia, G., Soldi-Lose, H. & Nahon, L. (2009). *Rev. Sci. Instrum.* **80**, 023102.

Giuliani, A., Jamme, F., Rouam, V., Wien, F., Giorgetta, J.-L., Lagarde, B., Chubar, O., Bac, S., Yao, I., Rey, S., Herbeaux, C., Marlats, J.-L., Zerbib, D., Polack, F. & Réfrégiers, M. (2009). *J. Synchrotron Rad.* **16**, 835–841.

Heimann, P. A., Koike, M., Hsu, C. W., Blank, D., Yang, X. M., Suits, A. G., Lee, Y. T., Evans, M., Ng, C. Y., Flaim, C. & Padmore, H. A. (1997). *Rev. Sci. Instrum.* **68**, 1945–1951.

Ito, K., Morioka, Y., Ukai, M., Kouchi, N., Hatano, Y. & Hayaishi, T. (1995). *Rev. Sci. Instrum.* **66**, 2119–2121.

Ito, K., Namioka, T., Morioka, Y., Sasaki, T., Noda, H., Goto, K., Katayama, T. & Koike, M. (1986). *Appl. Opt.* **25**, 837–847.

Ito, K., Ueda, K., Namioka, T., Yoshino, K. & Morioka, Y. (1988). *J. Opt. Soc. B*, **5**, 2006–2014.

Johnson, M., Bodi, A., Schulz, L. & Gerber, T. (2009). *Nucl. Instrum. Methods Phys. Res. A*, **610**, 597–603.

Klar, D., Harth, K., Ganz, J., Kraft, T., Ruf, M. W., Hotop, H., Tsemekhman, V., Tsemekhman, K. & Amusia, M. Y. (1992). *Z. Phys. D*, **23**, 101–113.

Koike, M., Heimann, P. A., Kung, A. H., Namioka, T., Digennaro, R., Gee, B. & Yu, N. (1994). *Nucl. Instrum. Methods Phys. Res. A*, **347**, 282–286.

Marcellus, P. de, Meinert, C., Nuevo, M., Filippi, J.-J., Danger, G., Deboffle, D., Nahon, L., Le Sergeant d'Hendecourt, L. & Meierhenrich, U. J. (2011). *Astrophys. J. Lett.* **727**, L27.

Marcouille, O., Brunelle, P., Chubar, O., Marteau, F., Massal, M., Nahon, L., Tavakoli, K., Veteran, J. & Filhol, J. M. (2007). *AIP Conf. Proc.* **879**, 311–314.

Matsui, T., Sato, H., Shimada, K., Arita, M., Senba, S., Yoshida, H., Shirasawa, K., Morita, M., Hiraya, A., Namatame, H. & Taniguchi, M. (2001). *Nucl. Instrum. Methods Phys. Res. A*, **467**, 537–540.

Meierhenrich, U. J., Filippi, J. J., Meinert, C., Hoffmann, S. V., Bredehöft, J. H. & Nahon, L. (2010). *Chem. Biodivers.* **7**, 1651–1659.

Mercier, B., Compin, M., Prevost, C., Bellec, G., Thissen, R., Dutuit, O. & Nahon, L. (2000). *J. Vac. Sci. Technol. A*, **18**, 2533–2541.

Milosavljević, A. R., Nicolas, C., Gil, J.-F., Canon, F., Réfrégiers, M., Nahon, L. & Giuliani, A. (2012). *J. Synchrotron Rad.* **19**, 174–178.

Milosavljević, A. R., Nicolas, C., Lemaire, J., Dehon, C., Thissen, R., Bizau, J. M., Réfrégiers, M., Nahon, L. & Giuliani, A. (2011). *Phys. Chem. Chem. Phys.* **13**, 15432–15436.

Nahon, L. & Alcaraz, C. (2004). *Appl. Opt.* **43**, 1024–1037.

Nahon, L., Alcaraz, C., Marlats, J. L., Lagarde, B., Polack, F., Thissen, R., Lepère, D. & Ito, K. (2001). *Rev. Sci. Instrum.* **72**, 1320–1329.

Nahon, L., Corlier, M., Peaupardin, P., Marteau, F., Marcouille, O., Brunelle, P., Alcaraz, C. & Thiry, P. (1997). *Nucl. Instrum. Methods Phys. Res. A*, **396**, 237–250.

Nahon, L., Garcia, G. A., Harding, C. J., Mikajlo, E. & Powis, I. (2006). *J. Chem. Phys.* **125**, 114309.

Nahon, L., Lagarde, B., Polack, F., Alcaraz, C., Dutuit, O., Vervloet, M. & Ito, K. (1998). *Nucl. Instrum. Methods Phys. Res. A*, **404**, 418–429.

Nahon, L., Polack, F., Lagarde, B., Thissen, R., Alcaraz, C., Dutuit, O. & Ito, K. (2001). *Nucl. Instrum. Methods Phys. Res. A*, **467**, 453–457.

Namioka, T. (1959). *J. Opt. Soc. Am.* **49**, 951–961.

Oliveira, N. de, Joyeux, D., Phalippou, D., Rodier, J. C., Polack, F., Vervloet, M. & Nahon, L. (2009). *Rev. Sci. Instrum.* **80**, 043101.

Oliveira, N. de, Roudjane, M., Joyeux, D., Phalippou, D., Rodier, J. C. & Nahon, L. (2011). *Nat. Photon.* **5**, 149–153.

Onuki, H. (1986). *Nucl. Instrum. Methods Phys. Res. A*, **246**, 94–98.

Petaccia, L., Vilmercati, P., Gorovikov, S., Barnaba, M., Bianco, A., Cocco, D., Masciovecchio, C. & Goldoni, A. (2009). *Nucl. Instrum. Methods Phys. Res. A*, **606**, 780–784.

Reichardt, G., Bahrdt, J., Schmidt, J. S., Gudat, W., Ehresmann, A., Muller-Albrecht, R., Molter, H., Schmoranzer, H., Martins, M., Schwentner, N. & Sasaki, S. (2001). *Nucl. Instrum. Methods Phys. Res. A*, **467**, 462–465.

Richard-Viard, M., Delboulbe, A. & Vervloet, M. (1996). *Chem. Phys.* **209**, 159–167.

Song, Y. F., Ma, C. I., Hsieh, T. F., Huang, L. R., Chung, S. C., Cheng, N. F., Hsiung, G. Y., Wang, D. J., Chen, C. T. & Tsang, K. L. (2001). *Nucl. Instrum. Methods Phys. Res. A*, **467**, 569–572.

Song, Y. F., Tseng, P. C., Huang, L. R., Chung, S. C., Dann, T. E., Chen, C. T. & Tsang, K. L. (2001). *Nucl. Instrum. Methods Phys. Res. A*, **467**, 496–499.

Tanaka, M., Yagi-Watanabe, K., Kaneko, F. & Nakagawa, K. (2009). *J. Synchrotron Rad.* **16**, 455–462.

Yao-Leclerc, I., Brochet, S., Chauvet, C., De Oliveira, N., Duval, J. P., Gil, J. F., Kubsky, S., Lagarde, B., Nahon, L., Nicolas, F., Silly, M., Sirotti, F. & Thomasset, M. (2011). *Proc. SPIE*, **8077**, 807712.

Yoshino, K. & Freeman, D. E. (1985). *J. Opt. Soc. B*, **2**, 1268–1274.